ISSN PRINT 2319 1775 Online 2320 7876

 UGC CARE Listed (Group -I) Journal Volume 11,Iss 11 , 2022

SYNTHESIS AND CHARACTERIZATION OF BARE AND RUTHENIUM-DOPED ZNO AND NIO: ASSESSING PHOTOCATALYTIC AND ANTIBIOFILM ACTIVITIES

RENIN F[1], Ph.D Research Scholar (Reg No: 20213012032007)

Department of Chemistry and Research Centre, Annai Velankanni College, Tholayavattam,

(Affiliated to Manonmaniam Sundaranar University, Abishekapatti, Tirunelveli, Tamil Nadu, India)

Email: renin.chem@gmail.com

DR. S R BRINTHA[2], Associate Professor,

Department of Chemistry and Research Centre, Annai Velankanni College, Tholayavattam,

(Affiliated to Manonmaniam Sundaranar University, Abishekapatti, Tirunelveli, Tamil Nadu, India)

ABSTRACT

Ruthenium-doped Zinc Oxide (ZnO) and Nickel Oxide (NiO) have garnered significant attention for their photocatalytic, and antibiofilm properties, presenting promising avenues for environmental and biomedical applications. This study presents a comparative analysis of the photocatalytic and antibiofilm activities of pure and ruthenium-doped ZnO and NiO. Synthesis methods, structural characterization, and performance evaluation were conducted to assess their effectiveness in photocatalytic degradation and antibiofilm efficacy. The results reveal distinct differences in the photocatalytic and antibiofilm behaviors of pure and ruthenium-doped ZnO and NiO, indicating the influence of dopant type and concentration on their performance. Insights from this comparative analysis provide valuable guidance for the rational design and optimization of metal-doped metal oxide-based photocatalysts and antibiofilm agents for diverse practical applications.

Keywords: Zinc Oxide ;Nickel Oxide; Ruthenium; doping; Antibiofilm Activity;Photocatalytic Dye Degradation;

1. Introduction

Zinc oxide (ZnO) is a broad bandgap semiconductor material that has garnered significant attention due to its potential applications in solar cells, light-emitting diodes, chemical sensors, surface acoustic wave filters, transparent conductors, and so on [1–7]. Zinc oxide has an energy gap of 3.37 eV and a large excitation binding energy of 60 meV.ZnO exhibits strong catalytic activity and photocatalysis, which aid in the degrad

ISSN PRINT 2319 1775 Online 2320 7876

 UGC CARE Listed (Group -I) Journal Volume 11,Iss 11 , 2022

ation of organic pollutants.It is a desirable biological choice due to its antibacterial pr operties [8]Another oxide material is nickel oxide (NiO), a semiconductor with a broadband gap (3.6–4.0 eV) that finds extensive application in electrochromic films, magnetic materials, gas sensing, catalysis, and battery cathodes [8–12]. These nanoparticles' low toxicity makes them suitable for usage in biological applications as well (Manigandan et al., 2019)There are numerous uses for the rare transition metal ruthenium (Ru). Due to its resistance to corrosion and tarnishing, as well as its catalytic properties, Ru is a good choice for a variety of chemical reactions. Because of its catalytic qualities in hydrogenation and dehydrogenation reactions, the chemical industry appreciates it especially. The antibacterial and anticancer characteristics of Ru compounds have also attracted interest in medicinal chemistry research [13].

The study outlines a simple precipitation route to synthesize these materials under ambient conditions. Characterization techniques such as XRD, FESEM, FTIR, and UV-Vis analysis are employed to assess the prepared samples' structural and optical properties. Additionally, the effectiveness of ruthenium doping in enhancing the properties of ZnO and NiO nanoparticles is investigated. Furthermore, the study delves into the photocatalytic, and antibiofilm activities of the synthesized samples, shedding light on their potential in environmental and biomedical applications.

2. Materials and methods

2.1 Pure ZnO nanoparticle synthesis

Precipitation was used to create bare ZnO nanoparticles. To precipitate off the zinc hydroxide, 0.1M sodium hydroxide was added dropwise to 0.1M zinc nitrate while being continuously stirred. After washing, this was calcined for four hours at 500°C and dried for twelve hours at 80°C.

2.2 Bare NiO nanoparticle synthesis

The process used to create bare NiO nanoparticles was similar. Nickel oxide (NiO) particles precipitated when 0.1 M sodium hydroxide was added dropwise while stirring continuously to 0.1 M nickel nitrate hexahydrate in deionized water. The precipitate was calcined at 500°C after it had settled and been cleaned with deionized water.

2.3 Synthesis of Ru-doped ZnO and NiO nanoparticles

To the zinc nitrate and nickel nitrate hexahydrate solutions, ruthenium trichloride solutions were mixed homogeneously before adding sodium hydroxide solutions to yield precipitates of dopants of ZnO and NiO nanoparticles. Similar to the control samples, the precipitates were washed with deionized water and calcined at 500°C.

ISSN PRINT 2319 1775 Online 2320 7876

 UGC CARE Listed (Group -I) Journal Volume 11,Iss 11 , 2022

2.4 Characterization

A variety of characterization techniques were used to examine the properties of the produced bare and Ru-NiO and Ru-ZnO nanoparticles and confirm their production. FTIR (Fourier Transform Infrared) spectroscopy was utilized to identify the various functional groups included in the created nanoparticles by examining the chemical bond vibrational modes that produce distinct peaks in the FTIR spectra [14]. Using a Bruker D2 Phaser, an X-ray diffraction (XRD) investigation was performed to confirm the successful synthesis of ZnO and its Ru-doped counterpart. The results provided important information about atomic spacing, crystallite size, and phase composition. Through the use of Field Emission-Scanning Electron Microscopy (FE-SEM), the size, morphological features, and physical form of the nanoparticles were investigated, offering insights into their nanoscale interactions [15].

To determine the elemental composition and purity of the produced pure and 1% Ru-ZnO and Ru -NiO nanoparticles, Energy-Dispersive X-ray Spectroscopy (EDAX) was used. A UV-Vis (ultraviolet-visible) spectrophotometer, which measures dye concentration quantitatively over time, was also used to track dye degradation under UV light irradiation to assess the photocatalytic efficacy of the nanoparticles [16].

2.5 Photocatalytic Dye Degradation

Four distinct dyes were used to assess the photocatalytic degradation activity of the produced 1% Ru-doped ZnO: Methylene Blue, Crystal Violet, Methyl Red, and Malachite Green. To prepare the dye solutions, a primary stock solution containing 1000 mg/L was diluted to the necessary concentration of 2.87 × 10-5 M. A predetermined amount of photocatalyst (1% Ru-doped ZnO) was added to the dye solution for each dye degradation experiment. One to twenty (12.5 mg of photocatalyst), one to fifty (25 mg), and one to one hundred (50 mg) were the three ratios of photocatalyst to dye that were employed. The liquid was put into a beaker that was used as a reaction vessel once the photocatalyst was added After that, the reaction vessel was subjected to UV light for a total of 120 minutes usi ng an 11W UV lamp.

Using the solution's absorbance as a gauge, the shift in dye concentration brought on by photocatalytic degradation was tracked during this time. A Systronics M2202 UV-Vis spectrophotometer operating at its maximum absorption wavelength was used to measure the absorbance. Then, using the absorbance drop from the first to the last time point, the % degradation of each dye was computed. To measure the degree of dye degradation, the absorbance peaks of the dyes at their wavelengths—Methylene Blue at 664 nm, Methyl Red at 430 nm, Malachite Green at 617 nm, and Crystal Violet at 590 nm—were tracked. Successful dye degradation over time is indicated by a decrease in absorbance, which suggests that the nanoparticles' photocatalytic activity is high. To determine how well the nanoparticles performed across various

ISSN PRINT 2319 1775 Online 2320 7876

 UGC CARE Listed (Group -I) Journal Volume 11,Iss 11 , 2022

dye molecules, the complete procedure was carried out individually for each of the four dyes [17].

2.6 Anti-Biofilm Test

To confirm the robustness and repeatability of the results, the anti-biofilm assay—a crucial step in determining how effective nanoparticles are at preventing the formation of bacterial biofilms—was painstakingly carried out in triplicate using the crystal violet method. The isolated bacterial strains, which included Escherichia coli and Staphylococcus aureus, were carefully cultured by inoculating them into Luria-Bertani (LB) broth. The resulting cultures were then carefully incubated for 16–18 hours at a controlled temperature of 37°C on a shaker incubator, guaranteeing the best possible conditions for bacterial growth and viability.

An exact volume of 198 µL of LB broth, carefully fortified with glucose to encourage bacterial growth, was methodically dispensed into each well in the sterile 96-well microtiter plate preparation. The target strains from the overnight bacterial culture were then carefully introduced to the designated wells in a pre-measured volume of 2 µL. Simultaneously, the material under examination was carefully added to the designated wells at different concentrations (0.25, 0.50, and 0.75 µL) to enable a thorough evaluation of its anti-biofilm action at different doses. After the careful inoculation procedure, the microtiter plates were carefully incubated for a carefully monitored period of 24 hours, which allowed the bacteria enough time to establish strong biofilms. To guarantee consistent and repeatable biofilm growth in each well during the incubation period, great effort was taken to maintain ideal environmental conditions, including temperature and humidity. Wells that contained simply the growing media and those that did not include nanoparticles functioned as careful blanks and controls, respectively, to offer crucial benchmarks for data interpretation.

Planktonic cells were carefully removed from the wells at the end of the incubation period in order to guarantee that only cells associated with biofilms were used in the analyses that followed. After carefully air-drying the wells, a 0.1% crystal violet dye solution was carefully added to each well, and the wells were left to incubate for a precisely timed interval of 15-20 minutes at room temperature. To ensure the accuracy and precision of the assay results, further careful washing steps with distilled water were performed to eliminate any excess color and unbound bacterial cells. A careful treatment with 33% glacial acetic acid was carefully applied to solubilize the crystal violet dye linked to the biofilm matrix, so releasing a detectable absorbance signal and making it easier to quantify the growth of biofilms. Last but not least, utilizing a cutting-edge microtiter plate reader, exact and quantitative absorbance readings were obtained at a wavelength of 600 nm, supplying information on the suppression of biofilm development mediated by the nanoparticles under study.

ISSN PRINT 2319 1775 Online 2320 7876

 UGC CARE Listed (Group -I) Journal Volume 11,Iss 11 , 2022

3. Results and discussion

3.1 UV-Visible spectroscopy

Figure 1 displays the UV-visible absorption spectra of pure and ZnO doped with 1% ruthenium. According to the literature, the undoped ZnO exhibits a single absorption peak at 383 nm, which is explained by the wide band gap semiconductor's band gap absorption. There are two distinct absorption peaks in the 1% Ru-doped ZnO spectrum: one at 275 nm and the other at 493 nm. These two peaks show that ruthenium has been successfully doped into the ZnO lattice. Much like the undoped sample, the peak at 275 nm represents the band gap absorption of ZnO. Ru ions may have been incorporated into the ZnO, which would explain the peak's shift when compared to the undoped ZnO lattice, which has the potential to influence the absorption spectra through the band gap energy [18].

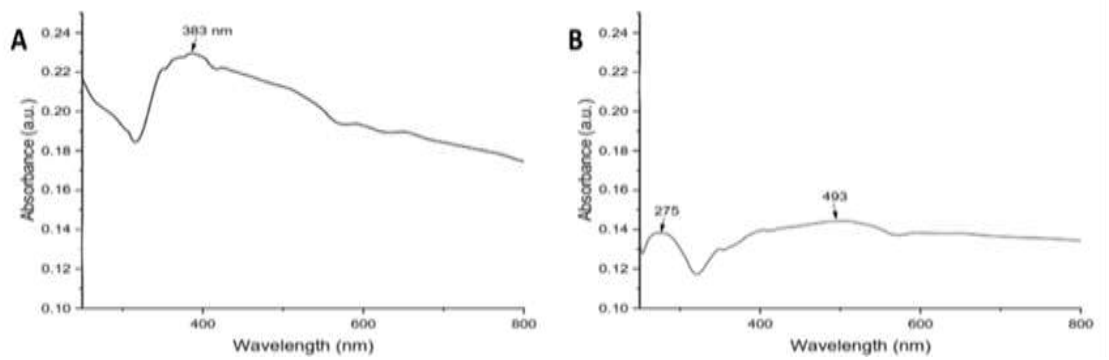

Figure 1: UV spectra showing the absorption maxima for (A) ZnO nanoparticles, (B) 1% Ru-doped ZnO nanoparticle

A comparable situation was noted when varying the concentration of ruthenium was added to NiO. Figure 2 displays the absorbance maxima of the undoped and 1% ruthenium-doped NiO nanoparticles. As in earlier research (Christy et al., 2021; Miri et al., 2022), the absorption peak at 296 nm (Figure 2A) may indicate the production of NiO nanoparticles. After doping with ruthenium, a blue shift was noticed. The shift in absorption maxima may be due to the introduction of Ru into the NiO lattice, the creation of intermediate energy levels, or the transfer of electrons from the 2p of oxygen to the 3d of nickel (Miri et al., 2022). The decrease in nanoparticle size and improved quantum confinement are also shown by the blue shift in the absorbance peak (Christy et al., 2021).

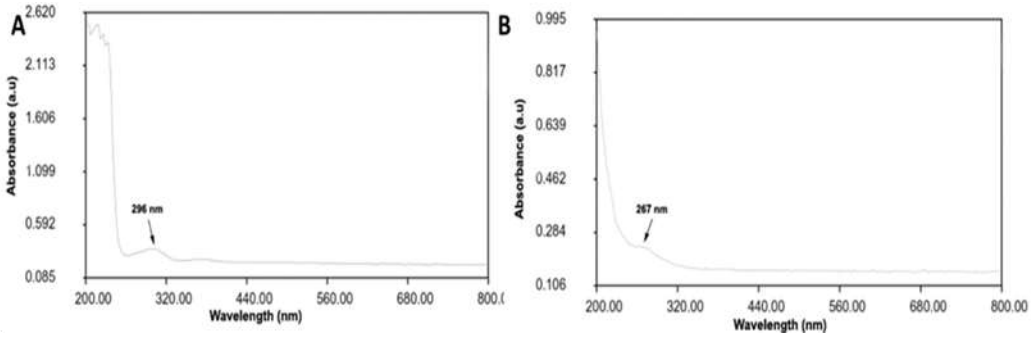

ISSN PRINT 2319 1775 Online 2320 7876

 UGC CARE Listed (Group -I) Journal Volume 11,Iss 11 , 2022

Figure 2: UV spectra showing the absorption maxima for (A) NiO nanoparticles, (B) 1% Ru-doped NiO nanoparticles

3.2 FTIR Analysis

Figure 3 displays the samples' FTIR spectra. The stretching vibrations of the hydroxyl (OH) groups adsorbed on the surface of the ZnO nanoparticles are responsible for the prominent peak at 3737 cm-1 for ZnO. The stretching vibration of Zn–O in the wurtzite structure of ZnO is shown by the peak at 598 cm-1. Additional peaks at 2360, 1786, 1510, 1357, 1104, and 836 cm-1 might be caused by the sample's absorbed water or trapped carbon dioxide vibrating. The signal at 1510 cm-1 disappearing in the case of 1% Ru-doped ZnO would indicate that Ru doping has changed the surface chemistry of ZnO. The observation of an increase in the intensity of the 598 cm-1 peak in Ru-doped ZnO could suggest that the Zn–O link within the ZnO lattice has been reinforced by Ru inclusion. According to this data, the observed changes in the material's characteristics are likely the result of Ru doping, which has altered the surface chemistry and strengthened the bonding strength in the ZnO lattice. Additional research may shed more light on the modifications brought about by Ru doping in the ZnO structure [19].

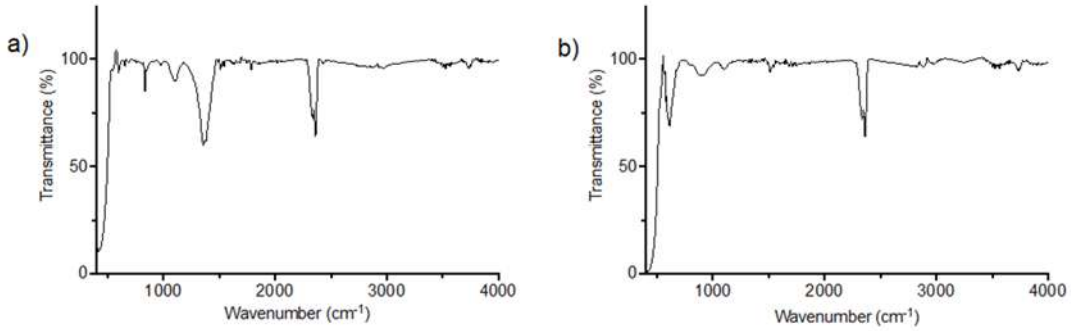

Figure 3 – FTIR spectra of a]ZnO and b]1% Ruthenium doped ZnO.

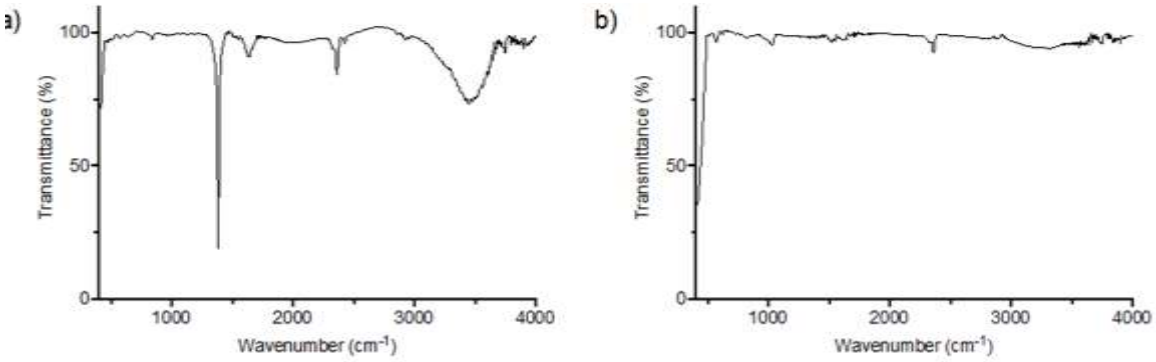

Figure 4– FTIR spectra of a] NiO and b]1% Ruthenium doped NiO.

ISSN PRINT 2319 1775 Online 2320 7876

 UGC CARE Listed (Group -I) Journal Volume 11,Iss 11 , 2022

Following doping, there was a widening and a shift in the spectra corresponding to the OH group from 3444 cm-1 to 3200 cm-1[figure 4], which suggests an interaction between the dopant and parent material. The doped nanoparticle lacked the peak at 1312 cm-1. H-bonding and the interaction of hydroxyl groups in both nanoparticles are responsible for the peaks at 2360 cm-1 and 1630 cm-1. The Ru-doped nanoparticle exhibits a large peak at 985 cm-1, which may be the result of Ru doping strengthening the Ni-O interaction. The trapped moisture may be the cause of the intense peak in the NiO nanoparticle at 1383 cm-1 (F & Brintha, 2023). The doped nanoparticle's peaks at 689 and 574 cm-1 and the undoped nanoparticle's peaks at 839 and 571 cm-1 indicate the presence of Ni-O bonds (Al Boukhari et al., 2019).

3.3 XRD Analysis

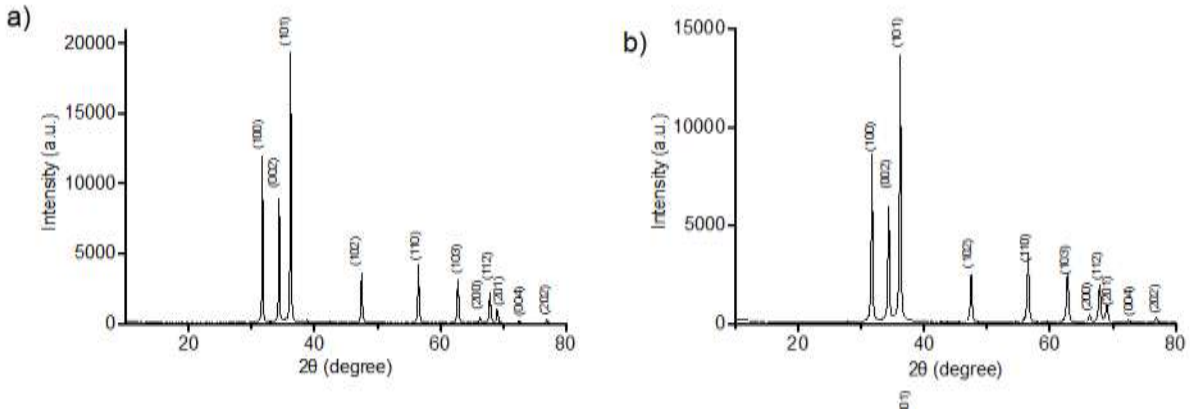

Figure 5 shows the X-ray diffraction patterns of a] ZnO and b]ZnO doped with 1% Ru.

In Fig 5,two-theta values of 31.734° (100 plane), 34.391° (002 plane), 36.212° (101 planes), 47.494° (102 plane), 56.534° (110 plane), 62.809° (103 plane), 66.312° (200 plane), 67.892° (112 plane), 69.023° (201 plane), 72.540° (004 plane), and 76.904° (202 plane) are the prominent diffraction peaks for both ZnO and Ru-doped ZnO. These peaks exhibit good alignment with JCPDS card No. 76-0704 (Joint Committee on Powder Diffraction Standards), suggesting the creation of ZnO with a hexagonal wurtzite structure. The Bruker TOPAS program was used to examine the lattice parameters, and ZnO had unit cell volume 47.588(5) Å³ with lattice parameters of a = 3.24925(16) Å and c = 5.2048(3) Å. With somewhat bigger lattice parameters (a = 3.25126(13) Å and c = 5.2071(2) Å), the 1% Ru-doped ZnO had a little larger unit cell volume (47.668(4) Å³). The effective integration of Ru ions into the ZnO lattice is responsible for the growth of the lattice parameters and unit cell volume of Ru-doped ZnO. Ru ions are larger than Zn ions, therefore their presence probably expands the lattice slightly, as seen by the higher unit cell volume and lattice parameters. In addition, it was found that the 1% Ru-doped ZnO had a smaller crystallite size—-40.45 nm compared to 30.46 nm for the undoped ZnO. The smaller crystallites that result from the incorporated Ru ions disrupting the crystal development may be the cause of this drop in crystallite size with Ru doping [20].

ISSN PRINT 2319 1775 Online 2320 7876

 UGC CARE Listed (Group -I) Journal Volume 11,Iss 11 , 2022

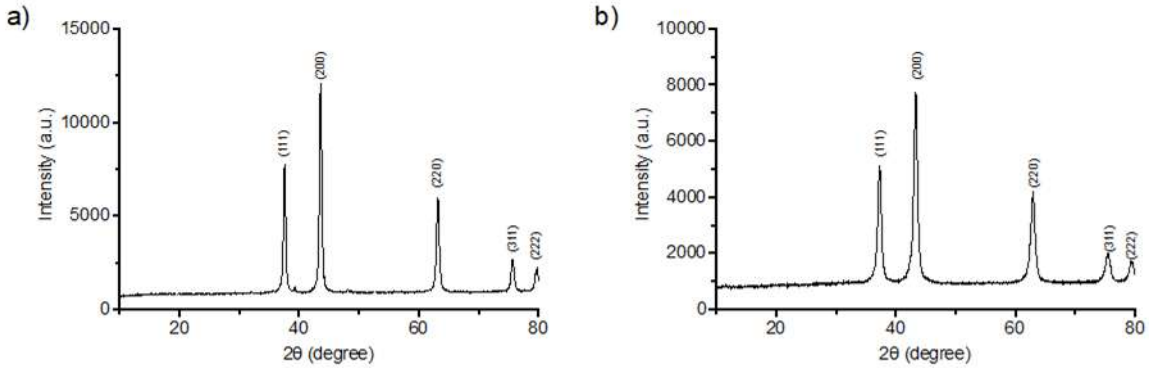

Figure 6 shows the X-ray diffraction patterns of NiO and NiO doped with 1% Ru

The X-ray diffraction (XRD) analysis, depicted in Figure 6, unveiled crucial insights into the structural properties of the nanoparticles. In the case of NiO nanoparticles (Figure 6a), distinct peaks were observed at 2θ values of 37.585°, 43.630°, 63.176°, and 75.725°. These specific angles correspond to the (111), (200), (220), and (311) hkl planes, respectively, indicative of the cubic lattice structure of NiO, as reported in the JCPDS file 01-1239 (Ali et al., 2022). Upon doping with ruthenium at concentrations of 1%, unique peaks emerged at 2θ values of 37.34°, 43.34°, 62.93°, and 75.54°respectively .These peaks signify the presence of ruthenium within the NiO lattice, altering its crystal structure and lattice parameters

3.4 FE-SEM and EDX Analysis

There are substantial differences between the produced ZnO and the 1% Ru-doped ZnO nanoparticles, as seen by the FE-SEM pictures (Figure 7a and b). In contrast to the Ru-doped ZnO nanoparticles, which are somewhat smaller around 50 nm, the ZnO nanoparticles have a size distribution in the range of 150 nm. The decrease in particle size following doping is in line with research, which frequently finds that doping refines particle size by impeding the growth of the parent particles. Reduced particle sizes can increase surface area, which could improve performance overall. of the nanoparticles in a range of uses, such as antibacterial, sensing, and catalysis.

The Energy-Dispersive X-ray (EDX) spectra (Figure 7) verify that both samples include oxygen (O) and zinc (Zn). It's interesting to note that the Ru-doped ZnO nanoparticles' EDX spectrum lacks a noticeable ruthenium (Ru) peak. This might be the result of the low concentration of Ru (1%), which might be below the EDX analysis's detection limit.

Moreover, the Ru atoms can be incorporated or replaced inside the ZnO lattice, which could complicate the EDX detection process. Not to be overlooked is the presence of gold (Au) peaks in the EDX spectra. This is a byproduct of the gold sputter coating procedure that was employed to get the samples ready for SEM imaging, not contamination. By preventing charging under the electron beam and increasing the

ISSN PRINT 2319 1775 Online 2320 7876

 UGC CARE Listed (Group -I) Journal Volume 11,Iss 11 , 2022

electrical conductivity of the materials, this procedure increases the quality of imaging [21].

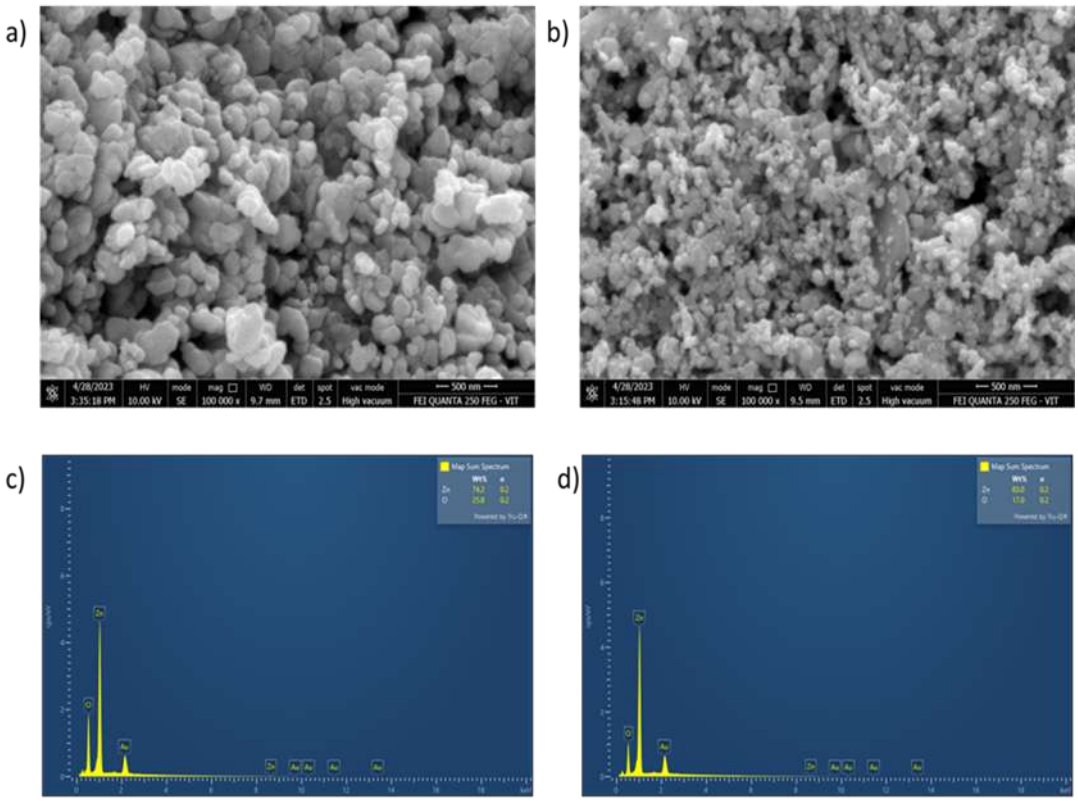

Figure 7 – FE-SEM image of a) ZnO, b) 1% Ru-Doped ZnO and EDX spectra of c) ZnO, d) 1% Ru-Doped ZnO

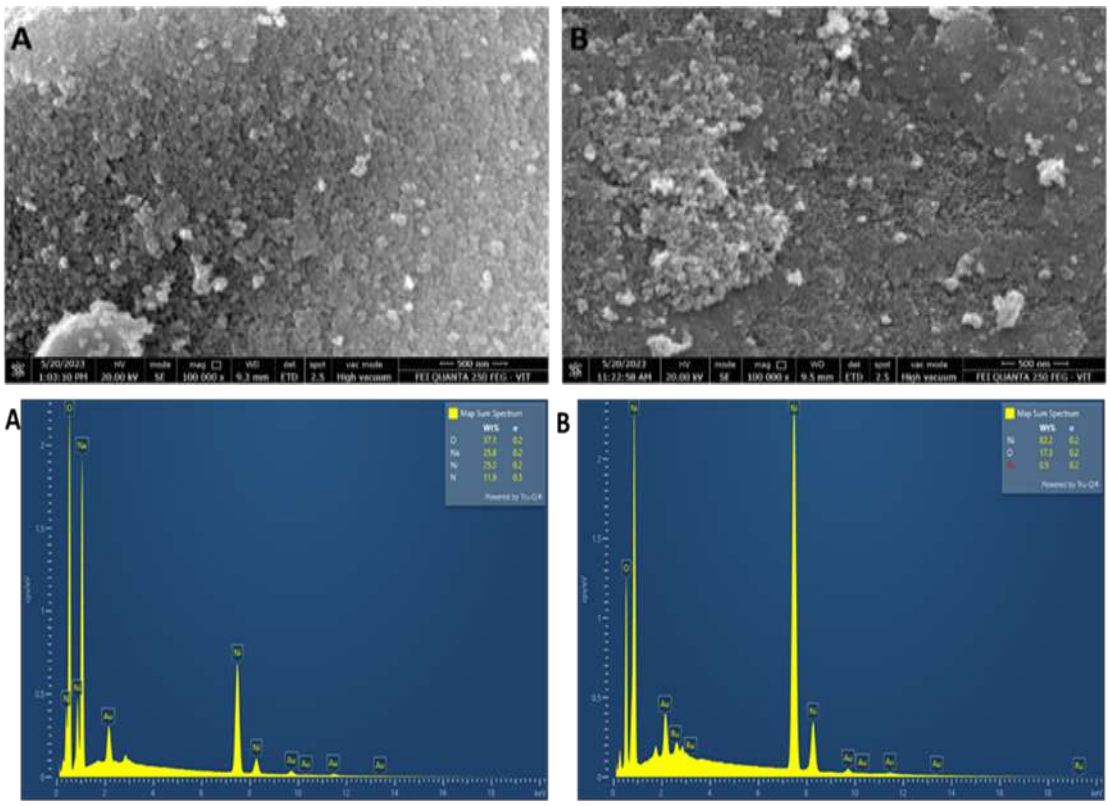

ISSN PRINT 2319 1775 Online 2320 7876

 UGC CARE Listed (Group -I) Journal Volume 11,Iss 11 , 2022

Figure 8 – FE-SEM image of A) NiO, B) 1% Ru-Doped NiO and EDX spectra of A]NiO and B]1% Ru-Doped NiO

Regarding the undoped NiO nanoparticles, spherical particles with an average size of around 40 nm were visible in the FESEM images (Figure 8A). Nevertheless, a discernible decrease in particle size was noted upon doping with 1% ruthenium, with the average size falling to 35 nm (Figure 8B). It is possible to explain the observed decrease in nanoparticle size in the ruthenium-doped samples to the effect of ruthenium doping, which seems to have a regulating effect on the initial growth of NiO nanoparticles. This implies that doping with ruthenium makes NiO nanoparticles more compactly arranged, which reduces their total size. All of the nanoparticles, irrespective of the doping concentration, had a spherical shape. When doped with ruthenium, the presence of ruthenium was detected in the spectra at weight percentages 0.5, 3 and 3.2% for 1% doped NiO (Figure 8B),

3.5. Photocatalytic activity

The results from the photocatalytic dye degradation experiments are shown in Figure 9 and the values are reported in Table 1. It could be observed that the Ru-doped ZnO showed a higher percentage of dye degradation for all dyes compared to pure ZnO nanoparticles indicating that Ru doping enhances the photocatalytic activity of ZnO . The photocatalytic activity of both ZnO and Ru-doped ZnO increases with the increase in the concentration of the catalyst, which is consistent with the theory as more catalyst surface area is available for the photocatalytic reaction.

Dye	**Photocatalyst**	**Percentage degradation**		
		12.5 mg	25mg	50mg
Crystal Violet	ZnO Nps	46.81	36.62	52.9
	1%Ru-ZnO Nps	59.21	50.86	65.45
	NiO Nps	25.03	35.73	38.79
	1% Ru-NiO Nps	36.4	43.3	55
Methyl Red	ZnO Nps	46.11	49.22	59.2
	1% Ru-ZnO Nps	49.24	62.8	64.26
	NiO Nps	22	28.05	32.37
	1% Ru-NiO Nps	31.4	38.2	43.7
Methylene	ZnO Nps	28.7	50.7	54.3

ISSN PRINT 2319 1775 Online 2320 7876

 UGC CARE Listed (Group -I) Journal Volume 11,Iss 11 , 2022

Blue				
	1% Ru-ZnO Nps	45.59	52.13	60.69
	NiO Nps	23.14	29.15	37.28
	1%Ru-NiO Nps	37.3	38.5	50
Malachite Green	ZnO Nps	60.54	60.08	52.2
	1% Ru-ZnO Nps	58.35	61.95	71.4
	NiO Nps	26.88	30.92	35.65
	1%Ru-NiO Nps	32.7	41.1	49.9

Table:1 Percentage degradation of dyes using the ZnO,NiO ,1% Ru doped ZnO and NiO nanoparticle photocatalysts.

The highest percentage of degradation was observed for a 50mg catalyst of 1% Ru-doped ZnO nanoparticles with values reaching 65% for crystal violet, 64% for methyl red, 60% for methylene blue and 71.5% for malachite green (Table 1). The percentage degradation was measured after 2 hours of treatment, which indicates that the rate of photocatalysis was commendable to that shown in the literature for ZnO nanoparticles (Nair et al., 2011; Qi et al., 2020). In the case of NiO nanoparticles, the percentage degradation of the dye using the photocatalysts NiO nanoparticles and 1% Ru-doped NiO nanoparticles are shown in Table 1. The values portray the enhancement in photocatalytic activity of the NiO nanoparticles upon doping with Ru (Table 1). It could also be noted that the Ru doping significantly reduced the particle size therefore more particles will be available for photocatalysis considering the same concentration of the undoped nanoparticles. The experimental values were found to be similar to those reported for NiO nanoparticles(Ghazal et al., 2020; Ghazal, Khandannasab, et al., 2021; Shkir et al., 2021).

ISSN PRINT 2319 1775 Online 2320 7876

 UGC CARE Listed (Group -I) Journal Volume 11,Iss 11 , 2022

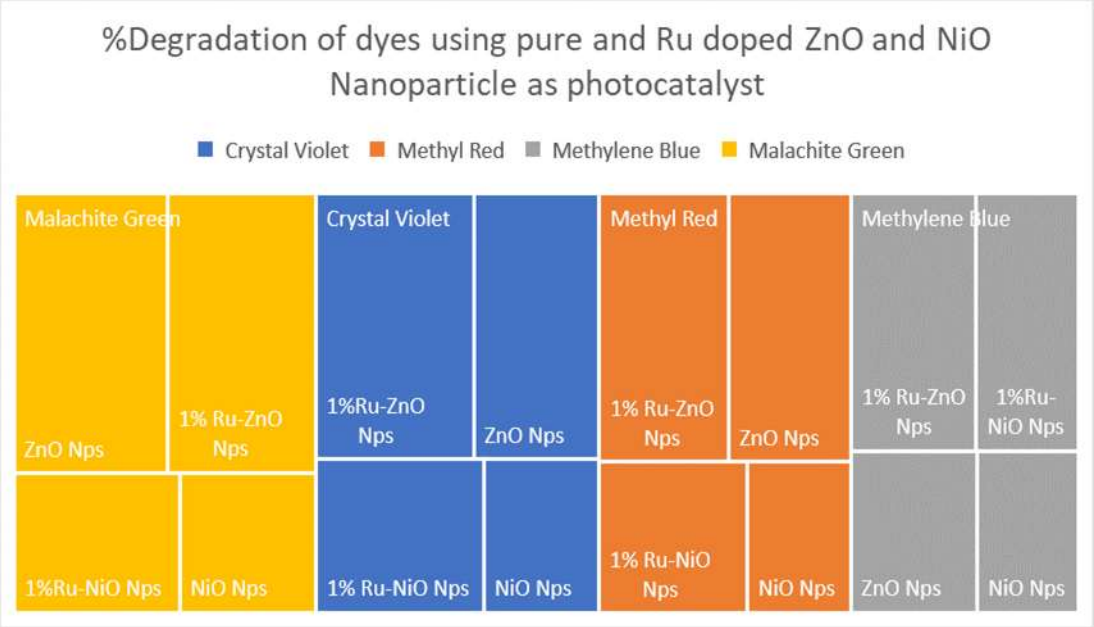

Figure 9: Percentage degradation of dyes Crystal violet, Methyl red, Methylene blue, and Malachite green using the ZnO, NiO,1% Ru doped NiO, and ZnO nanoparticle photocatalysts .

The deciding factor in photocatalysis is the interaction between the dye molecules and the photocatalyst (ZnO, NiO, or Ru-doped ZnO, Ru-doped NiO). Ruthenium doping markedly enhanced the photocatalysis, even though ZnO nanoparticles had a higher photocatalytic activity than NiO nanoparticles. The alteration in the electronic characteristics of the nanoparticles following Ru doping may have improved the charge separation and consequently enhanced the photocatalytic activity, explaining the difference in the degrading performance between the undoped and Ru-doped nanoparticles.

3.6. Biofilm Inhibition Assay

3.6.1Biofilm inhibition assay of ZnO and Ru-ZnO

The biofilm inhibition assay was designed to test if ZnO and Ru-doped ZnO nanoparticles could successfully stop Staphylococcus aureus (S. aureus) and Escherichia coli (E. coli) from developing biofilms. Table 2 and Figure 10 present the findings. The complex structures known as bacterial biofilms are created when closely spaced bacterial colonies are encased in a matrix of extracellular polymeric substance (EPS). Both in industrial and medicinal settings, these biofilms are linked to a variety of disorders. In the biofilm inhibition assay, E. Coli and S. aureus both showed complete biofilm formation, suggesting that the control group did not see a decrease in biofilm formation. On the other hand, when ZnO nanoparticle concentration increased, biofilm formation for both bacterial strains was observed to significantly decrease.

ISSN PRINT 2319 1775 Online 2320 7876

 UGC CARE Listed (Group -I) Journal Volume 11,Iss 11 , 2022

Concentration µg/mL	Biofilm Inhibition % of ZnO		Biofilm Inhibition % of Ru-doped ZnO	
	E.coli	S.aureus	E.coli	S.aureus
control	0	0	0	0
0.25 µg/mL	29	45	32	50
0.50 µg/mL	46	60	51	74
0.75 µg/mL	52	68	41	52

Table 2: Biofilm Inhibition % of ZnO and Ru-doped ZnO

On the other hand, both bacterial strains showed a marked increase and then decrease in biofilm formation as the concentration of 1% Ru-ZnO nanoparticles rose. In the case of E. coli, the biofilm inhibition percentage rose from 32% at 0.25 µg/mL to 51% at 0.50 µg/mL and reached a peak of 41% at 0.75 µg/mL. The percentage of biofilm inhibition for S. aureus also rose, rising from 50% at 0.25 µg/mL to 74% at 0.50 µg/mL before somewhat declining to 52% at 0.75 µg/mL. According to these findings, 5% Ru-ZnO nanoparticles efficiently and concentration-dependently prevent E. Coli and S. aureus from forming biofilms. The antibacterial characteristics of Ru-ZnO nanoparticles, which interfere with bacterial adhesion and colonization on surfaces, are ultimately responsible for the observed suppression of biofilm formation.

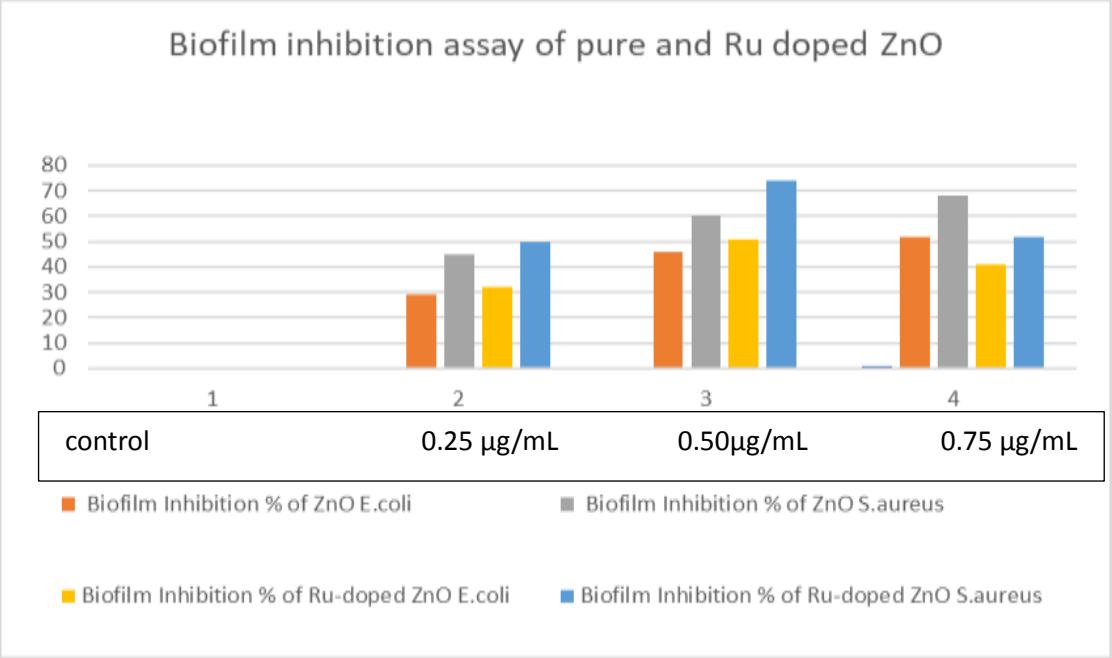

Figure10: Biofilm Inhibition % of ZnO and Ru doped ZnO

ISSN PRINT 2319 1775 Online 2320 7876

 UGC CARE Listed (Group -I) Journal Volume 11,Iss 11 , 2022

3.6.2 Antibiofilm activity of NiO and Ru-NiO

Concentration µg/mL	Biofilm Inhibition % of NiO		Biofilm Inhibition % of Ru-doped NiO	
	E.coli	S.aureus	E.coli	S.aureus
control	0	0	0	0
0.25 µg/mL	45	59	61	89
0.50 µg/mL	56	69	44	48
0.75 µg/mL	64	76	41	53

Table 3. Anti-biofilm activity of pure and Ru-doped NiO against E. Coli and S. aureus

The experiment was repeated with the same two strains of bacteria, S. aureus, and E. Coli, to find the percentage of biofilm inhibition at different dosages of pure NiO and Ru-doped NiO nanoparticles. The findings, which were presented in Table 3 and Figure 11, demonstrated the various degrees of biofilm reduction that the NiO nanoparticles were able to achieve. At 0.25 µg/ml, the nanoparticles showed notable biofilm suppression, with inhibition percentages of 59% for S. aureus and 45% for E. Coli. As the concentration increased to 0.50 µg/ml, the inhibition percentages for E. Coli and S. aureus increased to 56% and 69%, respectively. When the concentration was raised to 0.75 µg/ml, the inhibition percentages for S. aureus and E. Coli rose slightly to 76% and 64%, respectively. However, The Ru- NiO nanoparticles demonstrated noteworthy biofilm inhibition at 0.25 µg/ml, demonstrating inhibition percentages of 61% for E. Coli and 89% for S. aureus. The inhibition percentages dropped to 48% for E. Coli and 44% for S. aureus as the concentration rose to 0.50 µg/ml. The inhibition percentages for E. Coli and S. aureus decreased somewhat to 41% and 53%, respectively, upon further concentration increases to 0.75 µg/ml. These results imply that the nanoparticles successfully prevent the formation of biofilms in strains of E. Coli and S. aureus, with the greatest inhibition occurring at lower concentrations. However, it seems that with larger nanoparticle concentrations, the effectiveness of biofilm inhibition decreases.

ISSN PRINT 2319 1775 Online 2320 7876

 UGC CARE Listed (Group -I) Journal Volume 11,Iss 11 , 2022

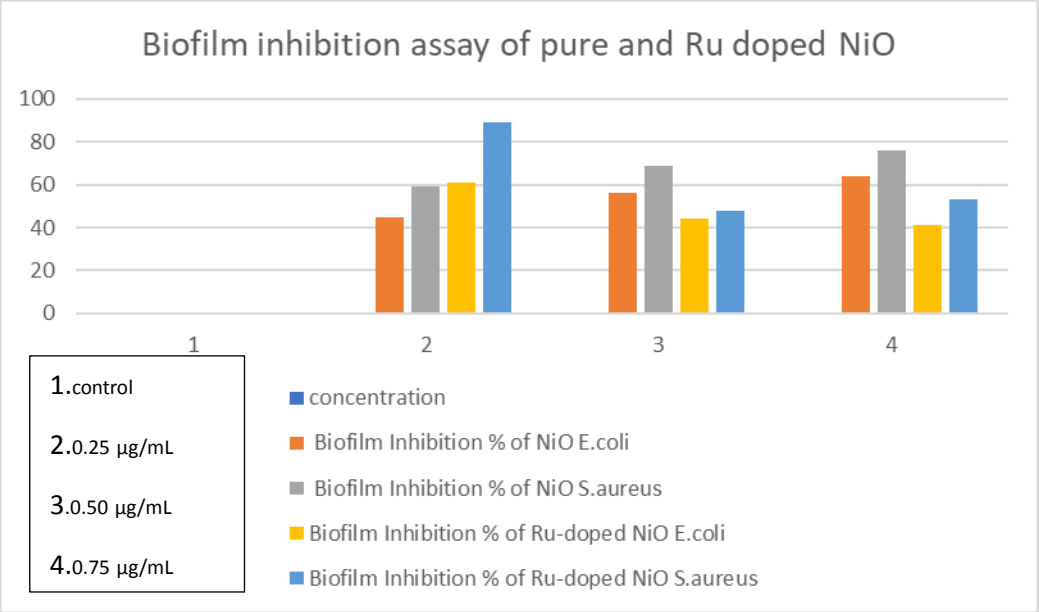

Figure11: Biofilm Inhibition % of NiO and Ru-doped NiO Nanoparticles

Conclusion:

This work assessed the doping of zinc oxide and nickel oxide nanoparticles with the rare transition metal ruthenium to improve the parent materials' characteristics. After successfully synthesizing and characterizing undoped ZnO, NiO, and 1% Ru-doped ZnO and NiO nanoparticles, their possible uses in antibiofilm activity, and photocatalytic dye degradation were assessed. XRD and SEM tests verified the shape and crystalline structure of the nanoparticles. Compared to pure ZnO and NiO, the doped nanoparticles showed a notable reduction in crystallite size, suggesting that the increased surface area could lead to possible improvements in surface activity. Ru doping also resulted in the creation of new absorption peaks to the UV-Vis spectra, which suggested modifications to the electronic structure and consequently the possibility of increased photocatalytic activity. In contrast, the antibiofilm activity of the doped nanoparticles was greater at lower concentrations than that of the undoped equivalent. In the case of doped nanoparticles, the photocatalytic activity was increased, creating opportunities for their use in the management of dye waste.

References

[1] A. Di Mauro, M. Cantarella, G. Nicotra, V. Privitera, and G. Impellizzeri, “Low-temperature atomic layer deposition of ZnO: applications in photocatalysis,” Applied Catalysis B: Environmental, vol. 196, pp. 68–76, 2016.

[2] U. ¨ Ozg ¨ ur, Y. I. Alivov, C. Liu et al., “A comprehensive review of ¨ ZnO materials and devices,” Journal of Applied Physics, vol. 98, no. 4, Article ID 041301, pp. 1–103, 2005.

ISSN PRINT 2319 1775 Online 2320 7876

 UGC CARE Listed (Group -I) Journal Volume 11,Iss 11 , 2022

[3] D.-J. Lee, H.-M. Kim, J.-Y. Kwon, H. Choi, S.-H. Kim, and K. B. Kim, "Structural and electrical properties of atomic layer deposited Al-doped ZnO films," Advanced Functional Materials, vol. 21, no. 3, pp. 448–455, 2011.

[4] S. Kerli, O. Akg ¨ ul, and ¨ U. Alver, "ZnO/TiO ¨ 2 particles and their solar cell application," AIP Conference Proceedings, vol. 1722, no. 1, Article ID 280002, 2016.

[5] I. Udom, M. K. Ram, E. K. Stefanakos, A. F. Hepp, and D. Y. Goswami, "One dimensional-ZnO nanostructures: synthesis, properties and environmental applications," Materials Science in Semiconductor Processing, vol. 16, no. 6, pp. 2070–2083, 2013.

[6] K. U. Iwu, V. Strano, A. Di Mauro, G. Impellizzeri, and S. Mirabella, "Enhanced quality, growth kinetics, and photocatalysis of ZnO nanowalls prepared by chemical bath deposition," Crystal Growth & Design, vol. 15, no. 9, pp. 4206–4212, 2015.

[7] A. Di Mauro, M. Zimbone, M. Scuderi, G. Nicotra, M. E. Fragala, and G. Impellizzeri, "Effect of Pt nanoparticles on the ` photocatalytic activity of ZnO nanofibers," Nanoscale Research Letters, vol. 10, no. 1, article 484, pp. 1–7, 2015

[8] Alshammari, B. H., Lashin, M. M., Mahmood, M. A., Al-Mubaddel, F. S., Ilyas, N., Rahman, N., ... & Khan, R. (2023). Organic and inorganic nanomaterials: fabrication, properties and applications. RSC advances, 13(20), 13735-13785.

[9] Q. Xia, H. Zhao, Y. Teng, Z. Du, J. Wang, and T. Zhang, "Synthesis of NiO/Ni nanocomposite anode material for high rate lithium-ion batteries," Materials Letters, vol. 142, pp. 67–70, 2015.

[10] Q. X. Xia, K. S. Hui, K. N. Hui, et al., "A facile synthesis method of hierarchically porous NiO nanosheets," Materials Letters, vol. 69, pp. 69–71, 2012.

[11] Y. Zhang, J. Wang, H. Wei, et al., "Hydrothermal synthesis of hierarchical mesoporous NiO nano urchins and their supercapacitor application," Materials Letters, vol. 162, pp. 67–70, 2016.

[12] H. Wei, W. Guo, Y. Sun, Z. Yang, and Y. Zhang, "Hot-injection synthesis and characterization of quaternary Cu2ZnSnSe4 nanocrystals," Materials Letters, vol. 64, no. 13, pp. 1424–1426, 2010

[13] Lawrence, M. A., Bullock, J. L., & Holder, A. A. (2018). Basic Coordination Chemistry of Ruthenium. Ruthenium Complexes: Photochemical and Biomedical Applications, 25-41.

[14]. Vasconcelos, S. C., Marchini, L., Lima, C. G., Madriaga, V. G., Ribeiro, R. S., Rossa, V., ... & Lima, T. M. (2022). Single-atom catalysts for the upgrading of biomass-derived molecules: an overview of their preparation, properties and applications. Green Chemistry, 24(7), 2722-2751.

[15]. Panda, M. K., Dhal, N. K., Kumar, M., Mishra, P. M., & Behera, R. K. (2021). Green synthesis of silver nanoparticles and its potential effect on phytopathogens. Materials Today: Proceedings, 35, 233-238.

[16]. Malekzadeh, M. (2021). Laser Pyrolysis Synthesis of Novel Nanomaterials Using Ultrasonic Spray-Based Precursor Delivery (Doctoral dissertation, State University of New York at Buffalo).

ISSN PRINT 2319 1775 Online 2320 7876

 UGC CARE Listed (Group -I) Journal Volume 11,Iss 11 , 2022

[17] . Tang, S., & Zheng, J. (2018). Antibacterial activity of silver nanoparticles: structural effects. Advanced healthcare materials, 7(13), 1701503

[18]Ahmad, M., Ahmed, E., Ahmed, Z., Arshad, M., Awan, M. S., Khan, Z. R., ... & Mahmood, K. (2020). Optical and structural analysis of ruthenium-doped ZnO nanoparticles synthesized by a green route. Materials Research Express, 7(11), 115003.

[19] Tanwar, A., Singh, R., & Kaur, I. (2019). Effect of ruthenium doping on structural and optical properties of ZnO nanoparticles. Journal of Materials Science: Materials in
Electronics, 30(19), 17634-17641

20.Wang, Z., Hu, S., Ma, J., Chen, C., Zhao, S., Wang, J., & Liu, X. (2019). Influence of ruthenium doping on the structural, electrical, and optical properties of ZnO thin films prepared by RF magnetron sputtering. Applied Surface Science, 487, 1232-1238.

[21]. Santhoshkumar, T., & Rajenderan, V. (2019). Synthesis, characterization, and catalytic applications of Ru-doped ZnO nanoparticles. Materials Today: Proceedings, 18, 1482-1488